

# Mechanical Resilience of Biofilms toward Environmental Perturbations Mediated by Extracellular Matrix

Qiuting Zhang, Danh Nguyen, Jung-Shen B. Tai, XJ Xu, Japinder Nijjer, Xin Huang, Ying Li, and Jing Yan\*

Biofilms are surface-associated communities of bacterial cells embedded in an extracellular matrix (ECM). Biofilm cells can survive and thrive in various dynamic environments causing tenacious problems in healthcare and industry. From a materials science point of view, biofilms can be considered as soft, viscoelastic materials, and exhibit remarkable mechanical resilience. How biofilms achieve such resilience toward various environmental perturbations remain unclear, although ECM has been generally considered to play a key role. Here, *Vibrio cholerae* (Vc) is used as a model organism to investigate biofilm mechanics in the nonlinear rheological regime by systematically examining the role of each constituent matrix component. Combining mutagenesis, rheological measurements, and molecular dynamics simulations, the mechanical behaviors of various mutant biofilms and their distinct mechanical phenotypes including mechanics-guided morphologies, nonlinear viscoelastic behavior, and recovery from large shear forces and heating are investigated. The results show that the ECM polymeric network protects the embedded cells from environmental challenges by providing mechanical resilience in response to large mechanical perturbation. The findings provide physical insights into the structure–property relationship of biofilms, which can be potentially employed to design biofilm removal strategies or, more forward-looking, engineer biofilms as beneficial, functional soft materials in dynamic environments.

## 1. Introduction

Biofilms are living soft materials in which bacterial cells act as active particles embedded in a 3D extracellular matrix (ECM).<sup>[1,2]</sup> Biofilm-dwelling cells are much more tolerant toward environmental challenges than isogenic cells in isolation,<sup>[1,3]</sup> thereby creating many tenacious problems in industry and in medicine. To design new biofilm removal strategies, it is crucial to understand the interplay between biofilm internal structure and material properties. On the other hand, biofilm is an important lifestyle of bacteria in a broad range of natural environments, and its unique material properties help biofilm-dwelling cells survive external challenges.<sup>[1,4]</sup> Studying biofilms from a mechanical standpoint thus enables us to understand how their robust mechanical properties contribute to cell viability and persistence under diverse environmental challenges, such as chemical insults, shear flows, pH changes, and temperature variations.<sup>[5–9]</sup> In addition, the understanding of biofilm mechanics is essential for biofilm removal and for using biofilms as beneficial, functional soft materials in

applications such as microbial fuel cells, bioremediations, and waste water purification.<sup>[10,11]</sup>


Recent biochemical studies suggest that the ECM, composed of polysaccharides, accessory proteins, and sometimes other components including extracellular DNAs, plays the key role in determining the functional and structural integrity of a biofilm.<sup>[1,12]</sup> The ECM polymeric network is responsible for gluing bacterial cells together to form a hydrated, gel-like, viscoelastic biomaterial and at the same time in anchoring the biofilm to a foreign surface. Therefore, the viscoelasticity and mechanical robustness of a biofilm is highly dependent on its ECM components.<sup>[13–17]</sup> On the other hand, several studies have also suggested the importance of the stiff ( $\approx$ MPa) bacterial cells in contributing to the biofilm rheology.<sup>[16,18,19]</sup> Recently, rheological techniques, including bulk or interfacial rheological measurements<sup>[13–16]</sup> and microrheology technique,<sup>[20]</sup> have been used to reveal the interplay between biofilm mechanical properties and their polymer networks. However, most rheological studies have focused on biofilm mechanics under small perturbations within the linear viscoelastic regime. Little is known about how polysaccharides and accessory proteins function together

Q. Zhang, J.-S. B. Tai, J. Nijjer, X. Huang, J. Yan  
Department of Molecular, Cellular and Developmental Biology  
Yale University  
C144 Yale Science Building, 260 Whitney Avenue, New Haven, CT 06520, USA  
E-mail: jing.yan@yale.edu

D. Nguyen, Y. Li  
Department of Mechanical Engineering and Polymer Program  
Institute of Materials Science University of Connecticut  
191 Auditorium Rd. U-3139, Storrs, CT 06269, USA

X. Xu  
Department of Physics  
Yale University  
217 Prospect St, New Haven, CT 06520, USA

J. Yan  
Quantitative Biology Institute  
Yale University  
C144 Yale Science Building, 260 Whitney Avenue, New Haven, CT 06520, USA

 The ORCID identification number(s) for the author(s) of this article can be found under <https://doi.org/10.1002/adfm.202110699>.

DOI: 10.1002/adfm.202110699

to provide biofilms high resilience to harsh, dynamic environmental challenges.

Here, we use *Vibrio cholerae* (Vc), a facultative human pathogen that can invade the intestinal mucosa and cause diarrhea,<sup>[12,21]</sup> as our model biofilm-forming organism. The well-defined genetics and biochemistry of the ECM components including Vibrio polysaccharide (VPS) and three associated matrix proteins (RbmA, Bap1, and RbmC) render Vc an appropriate model biofilm-former. By removing a single or a combination of matrix components from Vc biofilm, we systematically investigate how each ECM component contributes to the biofilm mechanical properties including nonlinear viscoelastic behavior and recovery after large deformation and heating. By combining mutagenesis, rheological measurements, and non-equilibrium molecular dynamics (NEMD) simulations, we demonstrate that the VPS network, reinforced by the accessory proteins, promotes mechanical resilience of Vc biofilm

when subjected to large shear forces and high temperature. By focusing on the large deformation region, we observed many mechanical features not observed before in the linear region. Our results show that bacteria employ the ECM polymeric network as a protective strategy to ensure mechanical stability and survival toward environmental challenges.

## 2. Results

### 2.1. Mechanics-Guided Biofilm Morphologies

The structure and main function of the major ECM components in Vc biofilm are shown in **Figure 1a**. Vc cells secrete VPS polymers to create a 3D ECM scaffold surrounding the cells; VPS is essential for Vc biofilm integrity and all accessory proteins rely on VPS to function.<sup>[22,23]</sup> The accessory protein RbmA

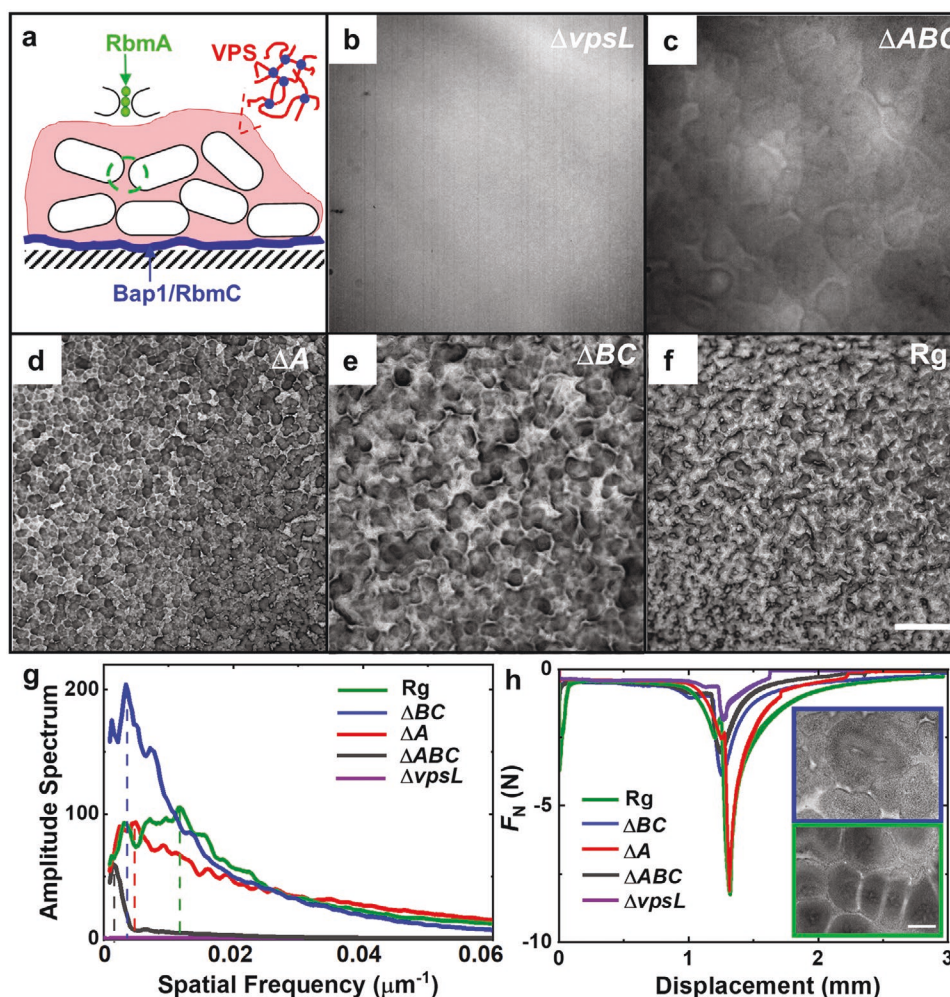


**Figure 1.** ECM components in Vc biofilms determine the morphologies of bacterial lawns. a) Schematic of the structure and functions of Vc matrix components. The white cylinders denote cells. The blue curvy lines (bottom) denote cell-to-surface adhesion via Bap1/RbmC. The red wavy lines denote VPS filling between cells. The green dots denote RbmA that connects neighboring cells. b–f) Representative images showing the surface morphologies of bacterial lawns from five different Vc strains. Scale bar: 500  $\mu\text{m}$ . g) Amplitude spectra for representative images in b–f) versus spatial frequency. h) Representative measurement of adhesion strength for each biofilm based on peel-off tests. Shown are the normal force  $F_N$  versus displacement during peeling-off of the biofilm from a surface. Insets are the magnified images of growing bacterial lawns, which show the different collision behaviors of microcolonies of  $\Delta BC$  (top) and Rg (bottom). Scale bar: 100  $\mu\text{m}$ .

dimerizes and interacts with VPS to connect neighboring cells.<sup>[24–26]</sup> Cell-to-surface adhesion is mediated by two other accessory proteins, Bap1 and RbmC,<sup>[27–29]</sup> which share high sequence and structural similarity. Bap1 and RbmC are also suggested to provide crosslinks to VPS.<sup>[16,27]</sup> To further dissect the function of each component in providing mechanical protection to cells, we generate a set of mutants lacking single or a combination of matrix components. This set of mutants enables us to systematically investigate how the biofilm mechanical behavior depends on various polymeric components. We use a rugose (Rg) strain background harboring a missense mutation in the *vpsC* gene (*vpsC*<sup>W240R</sup>) that elevates intracellular cyclic diguanylate levels,<sup>[30]</sup> leading to constitutive biofilm production. The Rg strain forms robust biofilms and thus allows us to focus on biomechanics rather than behaviors involving gene regulation. We further delete the flagella rotor *pomA* so that our results are not confounded by cell motility.<sup>[16]</sup>

We first grow a bacterial lawn on semisolid agar media to map the role of each gene in controlling the biofilm morphology at the air–solid interface (Figure S1, Supporting Information). We inoculate the agar plate with a low surface coverage such that the agar surface is colonized with discrete founder cells, which proliferate into small colonies that coalesce into a continuous layer. Similar to the morphogenesis of individual colony biofilms reported previously,<sup>[31]</sup> we find that the bacterial lawns also have surface topographies distinct for each mutant (Figure 1b–f). Based on a fast Fourier transfer (FFT) method, we analyze the spatial frequencies of each mutant biofilm (Figure 1g) and find that the characteristics of different mutants are distinguishable in the frequency domain. Specifically, we found that the wavelength extracted from FFT is inversely related to the stiffness of the biofilms (Figure S2, Supporting Information). First, the  $\Delta vpsL$  colonies remain liquid-like and pattern-less. This is because the  $\Delta vpsL$  mutant is unable to produce VPS and the constituent cells are in loose contact with each other in the colony (Figure 1a), much like a colloidal suspension. The  $\Delta rbmA\Delta bap1\Delta rbmC$  ( $\Delta ABC$ ) mutant produces VPS filling the space between neighboring cells but no accessory proteins (Figure 1a); this mutant also spreads easily on an agar plate and the corresponding bacterial lawn has slight surface height variations with a large wavelength around 640  $\mu\text{m}$ .

In addition to VPS, the extracellular proteins also play an important role in controlling the biofilm morphologies. In the  $\Delta rbmA$  ( $\Delta A$ ) mutant that produces cell-to-surface adhesion proteins and rugose (Rg) biofilms that produces all matrix components, densely packed colonies collide with one another to generate additional surface features, leading to smaller wavelengths ( $\approx 200$  and  $90\ \mu\text{m}$ , respectively) (Figure 1d,f). By contrast, in the  $\Delta bap1\Delta rbmC$  ( $\Delta BC$ ) mutant, the growing colonies can stack on top of each other during collision (Figure 1h insets; and Figure S3, Supporting Information) leading to a larger wavelength ( $\approx 290\ \mu\text{m}$ ). We hypothesize that this interesting behavior is due to the absence of surface adhesion in the  $\Delta BC$  mutant. To confirm this point, we qualitatively measure the surface adhesion by measuring the normal force needed to detach a biofilm from the underlying surface during the lifting of the top measurement shaft on the rheometer.<sup>[15,32]</sup> Indeed, the  $\Delta BC$  biofilm displays significantly smaller detachment force when compared to the  $\Delta A$  or the Rg biofilm (Figure 1h).

These results reinforce the idea in previous studies that Bap1 and RbmC are responsible for cell-to-surface adhesion and consequently control the biofilm morphologies,<sup>[27,31]</sup> although the mechanism at play in a bacterial lawn is different from that in an individual colony.

## 2.2. Nonlinear Viscoelastic Behavior

After demonstrating how ECM components guide the morphologies of bacterial lawn, we focus on the interplay between biofilm mechanics and each constituent matrix component using rheological measurements. While biofilm mechanics has been extensively documented in many biofilm-forming species including *V. cholerae*,<sup>[16]</sup> *Pseudomonas aeruginosa*,<sup>[13,14]</sup> *Staphylococcus epidermidis*,<sup>[33]</sup> *Bacillus subtilis*,<sup>[34]</sup> and many environmental biofilms,<sup>[17,35,36]</sup> most studies report measurements using the small amplitude oscillatory shear test (SAOS) within the linear viscoelastic regime (LVER).<sup>[37,38]</sup> In the LVER, the biofilm architecture remains unchanged after unloading, and the bulk material property is usually characterized by a few parameters such as storage modulus  $G'$  and loss modulus  $G''$ . Also, not much information can be gleaned after the yield point in these measurements. However, the natural environments are often more dynamic in which biofilms undergo large and rapid deformations corresponding to a high shear strain or strain rate. Moreover, large shear stresses are commonly applied to destroy biofilms or detach them from underlying surfaces in biofilm removal strategies in industrial and biomedical processes.<sup>[39]</sup> Under these conditions, the biofilm architecture will be significantly disturbed resulting in a nonlinear mechanical behavior. Therefore, SAOS measurement is insufficient to fully capture the viscoelastic behaviors of biofilms. The recently established large amplitude oscillatory shear test (LAOS)<sup>[40–42]</sup> provides an alternative approach to probe both the linear and nonlinear material response of biofilms.<sup>[17]</sup> Recently, Jana et al.<sup>[36]</sup> has employed this technique to characterize the nonlinear rheological behavior of biofilms from four different species and shown that they display distinct nonlinear viscoelasticity and energy dissipation in LAOS measurements. However, since the matrix components in these biofilms are vastly different from each other, it is difficult to draw mechanistic conclusions from a comparison across different species.

To fill this knowledge gap, we employ LAOS to characterize the nonlinear viscoelastic behaviors of the mutant biofilms in  $Vc$  that we generated earlier. We have previously reported the SAOS results for these mutants,<sup>[16]</sup> and we expect that extending the measurement to the nonlinear regime will reveal additional rheological signatures. During the LAOS test, biofilms are subjected to sinusoidal strain waveforms of increasing amplitude  $\gamma$ ; and the corresponding stress response  $\sigma$  as a function of time is recorded. As the strain amplitude increases beyond the LVER, the stress response transitions from sinusoidal (linear) to nonsinusoidal (nonlinear).<sup>[42]</sup> A convenient, geometrical presentation of the state of a material is to use a closed loop plot of  $\sigma$  versus strain  $\gamma$  or  $\sigma$  versus strain rate  $\dot{\gamma}$  by eliminating the parameter time  $t$ , which is known as the elastic or viscous Lissajous–Bowditch (L–B) plot, respectively. The L–B plots serve as a rheological fingerprint for each material. In



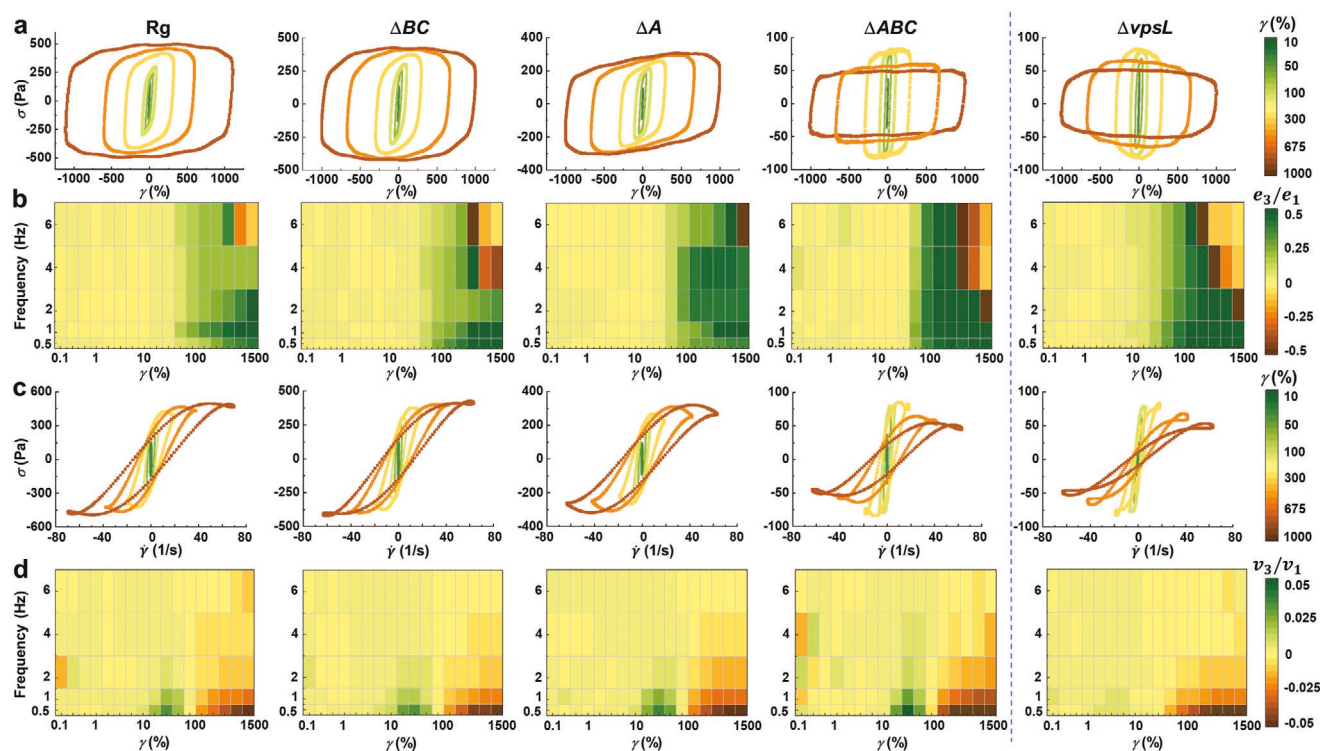


**Figure 2.** Nonlinear rheological characterization of Vc biofilms. a) Representative elastic Lissajous–Bowditch (L–B) plots for different mutant biofilms for strain amplitudes ranging from 10% to 1000% at a fixed oscillatory frequency (1 Hz). b) Representative heat maps of the normalized value  $e_3/e_1$  showing distinct regions in the Pipkin space<sup>[43]</sup> (a phase space of strain amplitude and frequency) where strain stiffening or softening happen. c) Representative viscous L–B plots for different mutants corresponding to the elastic L–B plots in a). d) Representative heat maps of the normalized value  $v_3/v_1$  show distinct regions in the Pipkin space where shear thickening or thinning occur.

the LVER, the elastic L–B plot displays an elliptical shape and the viscous L–B plot takes a circular shape; as the strain amplitude enters the nonlinear region, the elastic and viscous L–B plots become distorted into parallelogram-like and sigmoidal shapes, respectively. **Figure 2a** shows the elastic L–B plots for each of the tested strain from different Vc mutant biofilms at 1 Hz with strain amplitude ranging from 10% to 1000%. The elastic L–B plot for each mutant at a given strain amplitude takes a different shape and possesses a different total area that corresponds to the energy loss within one cycle. As the strain amplitude increases, a parallelogram-like shape emerges with a changing slope in the major axis characteristic of nonlinear material response. We observe that Rg,  $\Delta A$ , and  $\Delta BC$  biofilms have much larger maximum total stress ( $\approx 4$  times) signifying stiffer biofilms when compared to  $\Delta vpsL$  and  $\Delta ABC$  mutants. For larger strain amplitude ( $\gamma > 300\%$ ), the maximum stress of  $\Delta ABC$  biofilms decreases precipitously similar to the pattern in  $\Delta vpsL$ , suggesting that biofilms with an unstructured VPS are unable to withstand the extreme shear strain.

To quantitatively describe the material state based on the L–B plots, we use the MITlaos software<sup>[41,44]</sup> to calculate the first ( $e_1$  or  $v_1$ ) and the third ( $e_3$  or  $v_3$ ) order Chebyshev polynomial coefficients by approximating the shape of nonsinusoidal waveforms. The first-order Chebyshev polynomial coefficients describe the linear material response and are equivalent to the storage and loss moduli in SAOS. The third-order harmonic has a different physical meaning: a positive value indicates intracycle

strain stiffening or shear thickening, while a negative value indicates intracycle strain softening or shear thinning, respectively. The ratio of  $e_3/e_1$  for different mutants are plotted in the Pipkin diagram according to the given strain amplitude and frequency (Figure 2b). The transition to nonlinear response occurs at distinct locations in the pipkin diagram for different biofilms, which can help decipher the role of each constituent polymeric component of ECM and the interactions between them.

In the Pipkin space of  $e_3/e_1$ , all mutants initially show strain stiffening behavior ( $e_3/e_1 > 0$ ), followed by strain softening ( $e_3/e_1 < 0$ ) at larger imposed strain and higher frequency. Such intracycle strain stiffening behavior is not observed in prior SAOS measurement—in SAOS,  $G'$  stays nearly constant until it drops sharply after the yield point (Figure S2a, Supporting Information).<sup>[14,16]</sup> The transition from strain stiffening to softening appears at smaller strain amplitudes for higher frequencies. We find that such transitions in Rg and  $\Delta A$  biofilms take place at 6 Hz, with the peak values of  $e_3/e_1$  appearing in strain amplitude larger than 800%. In contrast, both the  $\Delta BC$  and  $\Delta ABC$  mutant biofilms start showing strain softening behavior at 4 and 2 Hz and the maximum values of  $e_3/e_1$  at 6 Hz occur slightly earlier at a strain amplitude around 400% compared to Rg and  $\Delta A$  biofilms. This result strengthens the idea proposed by earlier studies<sup>[16,27]</sup> that Bap1 and RbmC can reinforce the VPS polymer network, potentially through crosslinking, and thus endow Vc biofilms with the ability to resist larger shear forces. Furthermore, by comparing the nonlinear material

response of Rg and  $\Delta BC$  mutant biofilms to  $\Delta A$  and  $\Delta ABC$ , respectively, we observe that the mutants lacking RbmA display more pronounced strain-stiffening phenomenon, shown by a larger green area in the Pipkin diagram. We propose that this is because removing the RbmA-mediated cell-to-cell adhesion results in more expanded, looser biofilms,<sup>[24,26,45]</sup> which enables a higher degree of compression before close-packing of cells. Indeed, differential compressibility has previously been implied in biofilms with or without RbmA when they were subjected to osmotic compression.<sup>[46]</sup>

We further investigate the corresponding intracycle nonlinear viscous responses by plotting the viscous L–B curves and the ratio of  $v_3/v_1$  in the Pipkin diagram (Figure 2c,d). Similar to the elastic L–B plot, the viscous Lissajous curves show distorted sigmoidal shapes and the maximum stresses of  $\Delta vpsL$  and  $\Delta ABC$  biofilms experience a sudden decrease when subjected to a large strain amplitude. However, a large difference exists between the  $\Delta vpsL$  mutant missing the extracellular matrix and those that possess ECM: the hysteresis in the viscous L–B plot, shown by the area enclosed by viscous L–B curves, is much less for the  $\Delta vpsL$  mutant compared to any biofilm that contains VPS. We conjecture that this is because structural relaxation in the  $\Delta vpsL$  colony is nearly instantaneous involving only reorganization of rigid bacterial cells, whereas in the VPS-containing biofilms, the exopolysaccharides need longer time to relax. In the Pipkin space of  $v_3/v_1$ , it is observed that all biofilms initially exhibit shear thickening at lower strain amplitude, followed by shear thinning at higher strain amplitude; the transition however is much earlier for the  $\Delta vpsL$  mutant than the matrix-producing strains, which indicates that colonies from nonmatrix-producing cells are more susceptible to large deformations. Finally, we quantitatively analyze the L–B plots by calculating numerical values of intracycle strain stiffening index  $S$  and intracycle shear thickening index  $T$  (Figures S4 and S5, Supporting Information). Positive values of  $S$  or  $T$  indicate stiffening or thickening and negative values represent softening or thinning of materials. These measures ( $S$ ,  $T$ ) at different strain amplitudes and frequencies agree well with what we observed in the Pipkin diagram of the ratio of coefficients.

### 2.3. Nonequilibrium Molecular Dynamics (NEMD) Simulations

To gain physical insight into what internal structural rearrangement underlies the nonlinear material response of biofilms, we develop a NEMD model to capture the cellular configurations under various strain rates (Figure 3), based on our previous studies.<sup>[47,48]</sup> Our NEMD model treats the simulated biofilm as an aggregation of bacterial cells with attractive cell-to-cell interactions and applies periodic boundary conditions to the simulated biofilm. Note that the cell-to-cell interaction we used is *effective* in the sense that it includes contributions from cell-VPS and VPS-VPS interactions; recent work has shown that these more complicated interactions can be modeled efficiently using an effective intercellular potential.<sup>[9,49]</sup> 27 cells in total are randomly distributed and relaxed in a simulation box of  $10 \times 10 \times 10 \mu\text{m}^3$  before performing the sheared flow simulation. As shown in Figure 3a, starting from a random

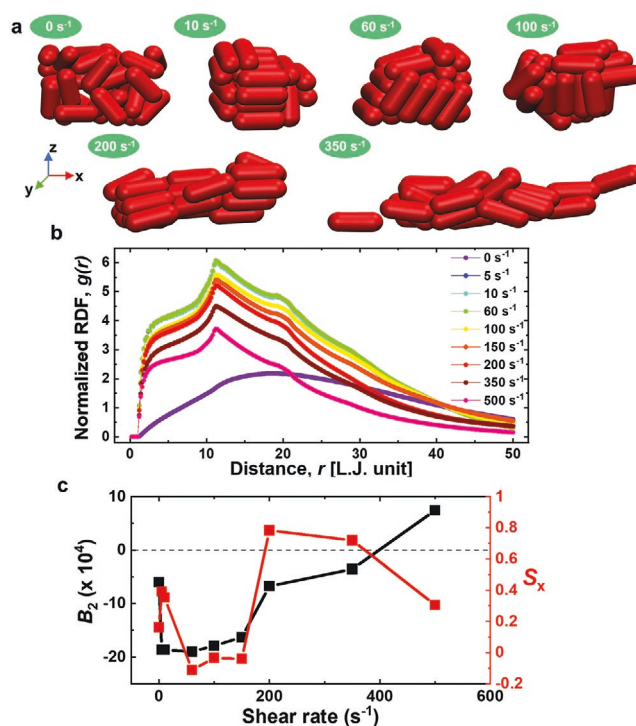


**Figure 3.** Molecular dynamics modeling of structural rearrangement in biofilms under shear. a) Snapshots of 27 bacterial cells under different shear rates ranging from 0 to 350 s<sup>−1</sup>. b) Radial distribution functions (RDF) of cells under various shear rates. c) Second virial coefficient  $B_2$  (black) and order parameter  $S_x$  (red) as a function of shear rate.  $B_2$  is calculated from the corresponding RDF in b). See text for definition and Method for calculation details.

organization (at 0 s<sup>−1</sup>), upon increasing the shear rate the simulated biofilm structure first becomes denser, and cells in the aggregate tend to align along the shear direction (at 60 s<sup>−1</sup>). However, at high shear rate, the biofilm cluster falls apart. The compactness of the bacterial cluster is quantified by the intercellular radial distribution function (RDF) (Figure 3b). Under no shear condition (purple curve, 0 s<sup>−1</sup>), there is no evident peak in the RDF curve. A small increase in shear rates (5 or 10 s<sup>−1</sup>) causes the cell aggregate to compact, leading to an emerging peak in RDF. When the shear rate goes up to 60 s<sup>−1</sup> (green curve), the amplitude of the peak reaches maximum, indicating the strongest aggregation. At higher shear rates, the cell aggregate tends to be more expanded, corresponding to the lower peak values of RDF when the shear rate varies from 100 s<sup>−1</sup> (yellow curve) to 500 s<sup>−1</sup> (pink curve). The lowest value of the RDF peak in our simulation is found at the highest shear rate (500 s<sup>−1</sup>) when the aggregate starts to break down. Overall, the compaction and aggregation behavior are reminiscent of hydrodynamic clustering in colloidal suspensions upon shear, which has been implicated to cause shear thickening of colloidal suspensions.<sup>[50]</sup>

To further quantify the degree of compaction and expansion as a function of shear rate, we calculated the second virial coefficient  $B_2$ ,<sup>[51]</sup> defined as  $B_2 = -0.5 \int (g(r) - 1) 4\pi r^2 dr$ , where  $g(r)$  is the corresponding RDF.  $B_2$  quantifies the effective intercellular interaction: a negative  $B_2$  corresponds to an effective attraction and a positive  $B_2$  corresponds to an effective

repulsion. As shown in Figure 3c, starting from the equilibrium value,  $B_2$  first becomes more negative due to shear-induced compaction, but turns positive when the bacterial cluster starts to fall apart. Meanwhile, to quantify the degree to which cells align with the shear direction, we define the cell ordering parameter  $S_x = 1/2(3|\bar{n}_i \cdot \bar{x}| - 1)$ , where  $\bar{n}_i$  represents the unit orientation director of each cell and the applied shearing direction is along the  $x$  axis.<sup>[52]</sup> Intriguingly,  $S_x$  shows a *nonmonotonic* behavior with multiple peaks. In the low shear region,  $S_x$  first increases when cells rotate individually toward the shear direction. However,  $S_x$  starts to decrease at  $10 \text{ s}^{-1}$ ; we interpret this behavior as being caused by cluster compaction, which impedes further cellular reorganization. Upon the onset of the cluster breakdown,  $S_x$  increases dramatically because cellular rearrangement becomes possible again. Indeed, comparing the cellular configurations at 100 and at  $200 \text{ s}^{-1}$  (Figure 3a), we observed that the cells start to reorganize to align with the shear direction but remain associated with each other at the peak value of  $S_x$ . Upon further increasing the shear rate, the cluster falls apart eventually (Figure S6, Supporting Information) and the cell alignment decreases again. In the limit of a well-dispersed state, we expect each isolated cell to tumble according to the Jeffery orbit<sup>[53,54]</sup> and there will be no net alignment on average. Therefore, the alignment of rod-shaped biofilm cells with flow is a collective phenomenon that reaches maximum at the onset of the cluster disassembly. Connecting the NEMD simulation to the experimental results, we conclude that cluster compaction and cell alignment serve as the underlying mechanism for intracycle shear hardening/thickening behavior observed at the intermediate shear amplitude in the LAOS measurement, and that cluster disassembly at high shear rate corresponds to the shear softening/thinning behavior at large amplitude. Indeed, converting the experimental parameters to shear rate shows that the transition shear rate from shear hardening to softening is comparable to what we observed in the simulation. For example, the hardening-to-softening transition takes place at  $\approx 190 \text{ s}^{-1}$  for the  $\Delta ABC$  biofilm, which is close to the prediction from the NEMD simulation ( $\approx 200 \text{ s}^{-1}$ ).

## 2.4. Mechanical Recovery After Large Shear Strain

Given that the biofilm microstructure is destroyed in the nonlinear viscoelastic regime, we are curious about the capability of biofilms to rebuild its structure afterward. In a previous study, *P. aeruginosa* biofilms have been reported to be able to fully recover after yielding.<sup>[13]</sup> However, the role of different matrix components in the recovery process remains unclear. Here, we study the recovery process in different mutant biofilms of *Vc* by measuring the storage modulus ( $G'$ ) as a function of time under oscillatory shear strain sweep test (Figure 4a). Similar to the thixotropy recovery test,<sup>[13,55]</sup> our test comprises three-step intervals with controlled strain amplitude at 1 Hz: First, a shear strain below the yield point is imposed on a biofilm to generate a linear material response without disrupting the microstructure;  $G'$  remains constant in the LVER. Next, as the shear strain increases beyond the yield point up to 1500%, the structure of the biofilms breaks down leading to a dramatic drop in  $G'$ . In the last step, the imposed strain decreases back to the LVER (0.1%) and the material restructuring process is monitored by following the recovery of  $G'$ . In this assay, we observe that  $G'$  recovers most of its initial value immediately except for the  $\Delta vpsL$  mutant. To quantitate this observation, we define the recovery ratio as the ratio between the value of  $G'$  60 s after yielding and the initial value. Figure 4b shows that the recovery ratio of  $\Delta vpsL$  mutant is less than 20%. In contrast, when VPS polymer fills the space between bacteria ( $\Delta ABC$  mutant biofilm),  $G'$  goes back to more than 60% of its original value within 60 s, indicating that the internal structure can be re-established easily. The cell-to-cell connection mediated by RbmA further boosts the recovery ability of  $\Delta ABC$  and Rg biofilms with higher recovery ratios over 80%. This finding suggests that biofilms with an ECM polymeric network possess typical thixotropic behavior with remarkable recovery properties in contrast to bacterial colonies without ECM, which promises biofilms as potential self-healing materials.

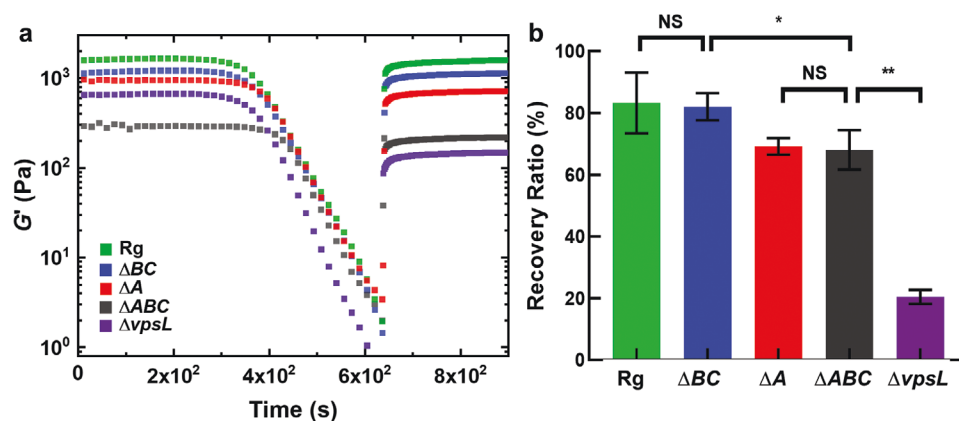


**Figure 4.** Mechanical recovery of *Vc* biofilms. a) Storage modulus  $G'$  as a function of time showing the recovery behavior of biofilms after the internal structure is destroyed by large shear strain. b) Recovery ratio for different biofilms after 60 s. Unpaired *t*-tests are used to perform statistical analyses. Error bars correspond standard deviation ( $n = 3$ ). NS denotes not significant; \*corresponds to  $p < 0.05$ ; \*\*  $p < 0.01$ .



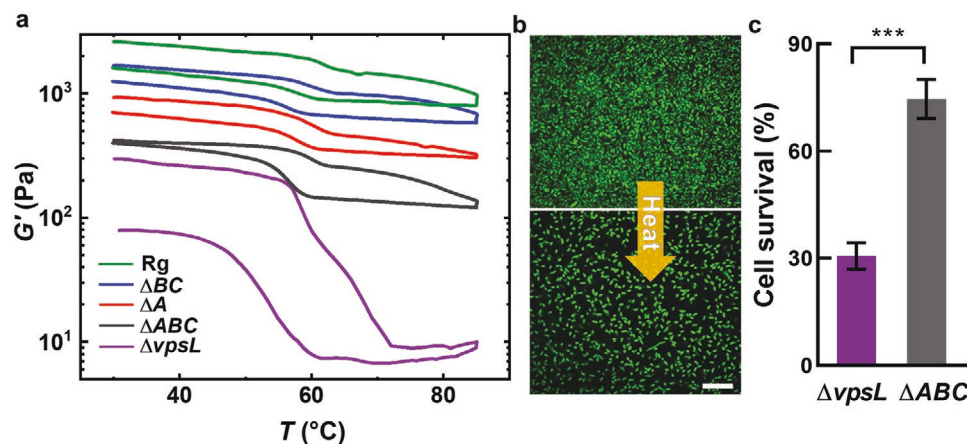


**Figure 5.** Resilience of Vc biofilms toward heat treatment. a) Storage modulus  $G'$  of different mutant biofilms versus temperature  $T$ . The samples were heated from 30 to 85 °C at a heating rate of 2 °C min<sup>-1</sup>, kept at 85 °C for 10 min, followed by cooling down from 85 to 30 °C at the same rate. b) Representative confocal images of  $\Delta vpsL$  culture before and after heating. Green signal corresponds to living cells (Syto9 staining). c) Percentage of cell survival on the surface after heating. \*\*\* denotes  $p < 0.001$ . Error bars correspond to standard deviations with  $n = 3$ .

## 2.5. Resilience toward Heat Treatment

So far, we have subjected biofilms to mechanical challenges. However, in nature, biofilms may encounter many other environmental fluctuations such as temperature changes. Moreover, heating is one of the most common and ancient practices to kill bacterial pathogens. It has been postulated that biofilms with a dense ECM polymeric network may show mechanical robustness toward temperature changes, which could complicate biofilm treatment.<sup>[8]</sup> To explore this aspect, we next investigate how temperature affects Vc biofilm mechanics. The effect of temperature on the linear viscoelastic behaviors of biofilm is shown in Figure 5a: We perform SAOS test with a temperature cycle from 30 to 85 °C and then back to 30 °C. As temperature increases,  $G'$  (at 1 Hz) drops dramatically around 60 °C but recovers partially to the origin value upon cooling. By comparing the temperature response of various mutant biofilms, we find that protein-mediated interactions within the matrix are not recoverable: the curves of  $R_g$ ,  $\Delta BC$ , and  $\Delta A$  biofilms do not close after heating. This is consistent with the well-known denaturing behavior of proteins upon heating. On the other hand, the  $\Delta ABC$  biofilm can fully recover its initial value, suggesting that polysaccharide-based interactions remain stable upon temperature cycling, consistent with the thermal stability of exopolysaccharides.<sup>[56]</sup> Interestingly, for the  $\Delta vpsL$  colony without any ECM,  $G'$  also displays a low recovery ratio around 30% after the temperature cycle. Because only direct cell-to-cell contacts are involved in the  $\Delta vpsL$  mutant, we hypothesize that the temperature-sensitivity of the  $\Delta vpsL$  colony arises from cell death, which reduces the number of cell-to-cell contacts. To test this hypothesis, we use a confocal microscope to visualize the change of structure in  $\Delta vpsL$  culture at single-cell level with DNA staining (Figure 5b). We observe that the cell number decreases dramatically, and a significant fraction of cells disappear, presumably through bursting, after heating at 85 °C for 10 min. To quantify this observation, we calculate the percentage of cell survival by comparing the areal fraction of surface covered by living cells before and after heating (Figure 5c). Interestingly, our result shows that compared to the  $\Delta ABC$  strain, cell viability in the

$\Delta vpsL$  strain is significantly reduced and the remaining percentage of cells is only around 30% after heating (vs 74% in the  $\Delta ABC$  culture). This comparison suggests that VPS, in addition to providing mechanical protection, also protects the embedded cells from heat to some extent. This may have implications for future design of heat-based biofilm treatment.

## 3. Discussion

In conclusion, we have systematically investigated the mechanical behaviors of a well-defined set of biofilm mutants in Vc under dynamic environments. We demonstrate that the formation of wrinkled morphologies of bacterial lawns are guided by both biofilm mechanics and biofilm-to-surface adhesion, which are in turn determined by the ECM components. By combining rheological measurements and dynamic modeling, we reveal how each individual matrix component gives rise to specific nonlinear viscoelastic behaviors, in particular during the transition from shear stiffening to softening. Using NEMD simulations, we reveal the microstructural changes that underlie the nonlinear biofilm mechanical behavior. We show that biofilm cells collectively align along the shear direction and pack more densely upon small shear, which explains the strain stiffening behavior in the LAOS measurements. Further increase of the shear rate leads to the breakdown of cell aggregates, corresponding to the observed strain thinning behavior. Finally, we have shown how the ECM polymeric network increases mechanical robustness and promotes cell viability under high temperature.

Compared to previous studies on biofilm rheology using SAOS,<sup>[13,14,16,33–35]</sup> some of which have used a systematic set of mutants,<sup>[14,16,34]</sup> our study in the nonlinear region reveals several unique mechanical features not observed before. First, with LAOS measurement, we observed that within one cycle a biofilm first strain stiffens ( $G'$  increases with shear strain) before yielding and strain softens afterward, and the transitions take place at different shear amplitudes for different mutants. This self-reinforcing response is potentially important for the

mechanical robustness of the biofilm in response to intermediate shear stress. Moreover, the viscous Lissajous plot has revealed the difference in the relaxation mode of colonies from matrix producing and nonproducer cells. Second, by comparing with results from NEMD simulations, we revealed the potential microstructural changes underlying the observed behavior of strain stiffening followed by strain softening in LAOS measurement. Third, in terms of the function of specific matrix component, we observed that in the Pipkin diagram, mutants lacking cell-to-cell connection conferred by RbmA shows a much larger area of strain stiffening compared to mutants with cell-to-cell connection. In contrast, in the previous SAOS measurement, the  $\Delta\text{rbmA}$  mutant biofilm simply shows a smaller plateau  $G'$ .<sup>[16]</sup> We expect that future development in the rheological techniques will generate more tools to understand the mechanical and structural features of biofilm. On the other hand, biofilms can also provide a testing ground for new rheological tools such as LAOS.

Many biofilm rheology studies so far have pointed out the importance of the extracellular matrix in conferring structural and mechanical integrity to a biofilm.<sup>[13,16,17]</sup> It is commonly assumed that the extracellular polymer plays the dominant role in defining biofilm rheology. However, recent progress in single-cell imaging of biofilms has shown that the biofilm-producing cells can occupy as much as 40% of the total biofilm space<sup>[9,57]</sup>; given the rigidity of bacterial cells,<sup>[58]</sup> their contribution to biofilm rheology cannot be neglected. In fact, although no specific attraction exists between the  $\Delta\text{vpsL}$  cells, the  $\Delta\text{vpsL}$  colony does show some viscoelastic signals similar to a dense colloidal suspension such as a transition from a viscoelastic solid to fluid as shear strain increases. The existence of the extracellular polysaccharides significantly modifies the transitions and the nonlinear rheological behaviors.

Biofilm matrix is chemically and functionally complicated.<sup>[1,4,59]</sup> Each constituent may contribute to biofilm rheology in a unique way and biofilms from different species may behave very differently—a generic, convergent scheme for biofilm rheology has yet to emerge. Using *Vc* as a model organism, we show that accessory proteins also play distinct roles in controlling biofilm mechanics: On the one hand, Bap1 and RbmC reinforce the VPS polymer network to resist external challenges. On the other hand, the lack of cell-to-cell adhesion protein RbmA extends the strain stiffening region—an effect that cannot be understood by simply attributing biofilm mechanics solely to the polymeric matrix. These findings confirm and extend many previous work on the *V. cholerae* biofilm matrix.<sup>[12,16,27]</sup>

By using new information provided by LAOS, coupled with dynamic simulations, our results represent a solid step toward understanding the structure–property relationship in biofilms. These understandings and technical tools could potentially be employed to develop generic strategies for disrupting harmful biofilms or harnessing biofilms as functional materials.<sup>[11,60]</sup> Our results also provide inspirations for materials scientists interested in designing new functional composites that rely on particulates and polymer matrix,<sup>[61–63]</sup> as *Vc* biofilms do. Future integration of our simulation model into agent-based simulations<sup>[64,65]</sup> will also shed light on how mechanics shapes the development of biofilm, a topic of significant recent interest.<sup>[9,66–68]</sup>

## 4. Experimental Section

**Strain and Media:** All *Vc* strains used in this study were derivatives of the wild-type *Vc* O1 biovar El Tor strain C6706. The rugose (Rg) strain harbors a missense mutation in the *vpvC* gene (*vpvC*<sup>W240R</sup>) that elevates intracellular cyclic diguanylate levels.<sup>[30]</sup> Additional mutations were genetically engineered into this strain through the suicide vector pKAS32.<sup>[69]</sup> A strain list is provided in Table S1 (Supporting Information). All strains were grown in lysogeny broth (LB) at 37 °C with shaking.

**Biofilm Growth on Agar Plates:** *Vc* strains were streaked on LB plates containing 1.5% agar and grown at 37 °C overnight. Individual colonies were inoculated into 3 mL of LB liquid medium containing glass beads, and the cultures were grown with shaking at 37 °C to mid-exponential phase (5–6 h). Subsequently, the cells in the cultures were mixed by vortex, OD<sub>600</sub> was measured, and the cultures were back diluted to an OD<sub>600</sub> of 0.5. 50  $\mu\text{L}$  of this inoculum was uniformly spread-plated onto prewarmed M9-agar plates (100 mm) supplemented with  $2 \times 10^{-3}$  M  $\text{MgSO}_4$ ,  $100 \times 10^{-6}$  M  $\text{CaCl}_2$ , and 0.5% glucose. Defined media was used instead of LB for biofilm culturing in this study because most of the recent biofilm structural characterizations were performed in this defined media.<sup>[57,67]</sup> Plates were then incubated at 37 °C with high humidity (90%) for 2 days to allow the biofilm to uniformly cover the entire plate.

**Microscopy:** Confocal images were acquired with a Yokogawa W1 confocal scanning unit (CSU) mounted on a Nikon Ti2-E inverted microscope with a Perfect Focus System, using a 4 $\times$  objective (N.A. = 0.2, for morphological analysis) or a 60 $\times$  water (N.A. = 1.2, for high-resolution imaging in temperature sweep experiment) for different experiments. For morphology characterizations, bright field images of *Vc* biofilms formed by different mutants were taken under the same illumination condition using a 4 $\times$  objective with a  $3.31 \times 3.31$  mm field of view and were used for Fourier analysis. For cell viability analysis in temperature test, a 488 nm laser was used to excite live cells stained with Syto9 nucleic acid stain ( $3.34 \times 10^{-6}$  M, LIVE/DEAD BacLight Bacterial Viability Kit).

**Rheological Measurement:** All rheological measurements were performed with a stress-controlled shear rheometer (Anton Paar Physica MCR502WESP). For each measurement, biofilms were collected with a pipette tip or a razor blade and transferred onto the lower plate of the rheometer.<sup>[16]</sup> Care was taken not to damage the agar surface to avoid inclusion of agar in the measurement; this is confirmed by visual inspection after scrapping. After sandwiching the biofilms between the upper and lower plates with a gap size of 0.5 mm, silicone oil (5 cSt at 25 °C, Sigma-Aldrich) was applied to enclose the biofilm to avoid water evaporation. The biofilms were allowed to relax for at least 5 min after loading before taking the measurement. Sandblasted surfaces were used in the shearing tests for both the upper and lower plates to avoid slippage at the boundary. Glass surfaces were used in the pulling test to measure the surface adhesion by lifting the top shaft at a constant velocity of  $10 \mu\text{m s}^{-1}$ . Note that the pulling test only qualitatively measure the adhesive strength due to the many other energy dissipation processes such as viscous losses involved in this process.<sup>[15,32]</sup> All rheological properties of the biofilm remained roughly constant for at least 48 h.

Oscillatory shear tests (SAOS and LAOS) were performed with increasing amplitude of the oscillatory strain  $\gamma$  from 0.01% to 1500% at the designated frequencies (0.5, 1, 2, 4, 6 Hz). The storage modulus  $G'$  and the loss modulus  $G''$  were extracted with the RheoPlus software as a function of  $\gamma$ . Meanwhile, the raw waveforms of strain ( $\gamma$ ) and stress ( $\sigma$ ) were recorded for further analysis. Subsequently, biofilms were subjected to a constant small strain amplitude 0.1% for more than 1 min to test the recovery ratio of  $G'$ .

Temperature sweep tests were performed in the LVER. The initial temperature was set as 30 °C. The  $G'$  was measured at a fixed frequency of 1 Hz and shear strain amplitude of 0.1%. The sample was first heated from 30 to 85 °C, kept at 85 °C for 10 min, and then cooled down from 85 to 30 °C. The heating/cooling rate was  $2 \text{ }^\circ\text{C min}^{-1}$  to ensure a homogeneous temperature across the sample.



**Simulation Procedure:** We study the effect of shear rate on the bacterial orientation and aggregation through NEMD simulations. All computational models of bacterial cells are implemented using a recently developed package by Ye and co-workers, which is highly efficient for fluid-structure interaction (FSI) simulations, the so-called OpenFSI.<sup>[70]</sup> Within this package, the bacterial cells are accounted for by a lattice model (LM) implemented in the framework of the Large-scale Atomic/Molecular Massively Parallel Simulator (LAMMPS).<sup>[71]</sup> In this study, the bacterial cell has a rod-like shape with a diameter of 1  $\mu\text{m}$  and a length of 3  $\mu\text{m}$  (length/diameter ratio = 3). The bacterial cell membrane is discretized into a point system with a triangular network of 4582 vertices and 9160 elements (Figure S6a, Supporting Information), similar to the red blood cell model.<sup>[72]</sup> The Lagrangian mesh of the cell membrane is approximately uniform, and the mesh size is about 50 nm. The membrane structure is immersed in an incompressible flow (water), which is solved using the Lattice Boltzmann Method (LBM) to efficiently solve the Boltzmann equation that is able to recover the Navier–Stokes equation in mesoscale.<sup>[70]</sup> The lattice spacing of fluid field  $d_x$  is chosen to be 0.1  $\mu\text{m}$ . Additionally, the immersed boundary method (IBM) is employed to couple LM and LBM together, accounting for the FSI.

The mechanical properties of the membrane are imposed by exerting potential functions on the triangular networks. The intermolecular interactions between bacterial cells include Morse potential for attractive interaction and a short-range Lennard Jones (LJ) potential for pure repulsion, which were introduced in recent works by Ye et al.<sup>[70,72]</sup> The bacterial cells are randomly placed in a simulation box of  $10 \times 10 \times 10 \mu\text{m}^3$ , in which periodic boundary conditions are applied in the x and y directions, while z-direction is bounded by two flat plates. The shear flow is driven in the x-direction by moving the z-top flat plate with different x-direction velocities calculated from the shear rate values with the formula  $v_{\text{top}} = \text{shear rate} \times \text{channel height}$ . All simulation and physical parameters are summarized in the Table S2 (Supporting Information). All snapshots derived from the simulations are rendered using Visual Molecular Dynamics (VMD) software.<sup>[73]</sup>

**RDF Measurement:** The radial distribution of bacterial cells was quantified as the number density  $g(r)$  in which  $r$  denotes the radial direction between the nodes of different cells. The channel along the radial direction was split into small identical bins with size  $dr$ . Due to the anisotropic geometry of the cell, the center of mass was not used for calculating the cell–cell distance; instead, the node–node distance was calculated between different cells and counted the number of nodes locating inside these bins and denoted it as  $n_{\text{NP}}$ . Finally,  $g(r) = \frac{n_{\text{NP}}}{V \cdot N_{\text{nodes}}}$  was calculated, where  $V$  is the volume of the bin and  $N_{\text{nodes}}$  is the total number of nodes in the channel.

## Supporting Information

Supporting Information is available from the Wiley Online Library or from the author.

## Acknowledgements

The authors thank the help from Dr. Rong Long, Dr. Alison Sweeney, and Dr. Antonio Perazzo for helpful discussions. J.Y. holds a Career Award at the Scientific Interface from the Burroughs Wellcome Fund. Y.L. would like to thank the support by the National Science Foundation under the Grant Nos. OAC-1755779 and CMMI-1762661.

## Conflict of Interest

The authors declare no conflict of interest.

## Data Availability Statement

The data that support the findings of this study are available from the corresponding author upon reasonable request.

## Keywords

biofilms, environmental perturbations, nonlinear viscoelasticity, rheology, soft materials

Received: October 21, 2021

Revised: December 19, 2021

Published online:

- [1] H.-C. Flemming, J. Wingender, *Nat. Rev. Microbiol.* **2010**, *8*, 623.
- [2] L. Hall-Stoodley, J. W. Costerton, P. Stoodley, *Nat. Rev. Microbiol.* **2004**, *2*, 95.
- [3] A. Dragoš, Á. T. Kovács, *Trends Microbiol.* **2017**, *25*, 257.
- [4] H.-C. Flemming, T. R. Neu, D. J. Wozniak, *J. Bacteriol.* **2007**, *189*, 7945.
- [5] J. M. Vroom, K. J. De Grauw, H. C. Gerritsen, D. J. Bradshaw, P. D. Marsh, G. K. Watson, J. J. Birmingham, C. Allison, *Appl. Environ. Microbiol.* **1999**, *65*, 3502.
- [6] P. S. Stewart, M. J. Franklin, *Nat. Rev. Microbiol.* **2008**, *6*, 199.
- [7] S. M. Boomer, K. L. Noll, G. G. Geesey, B. E. Dutton, *Appl. Environ. Microbiol.* **2009**, *75*, 2464.
- [8] L. Pavlovsky, R. A. Sturtevant, J. G. Younger, M. J. Solomon, *Langmuir* **2015**, *31*, 2036.
- [9] R. Hartmann, P. K. Singh, P. Pearce, R. Mok, B. Song, F. Díaz-Pascual, J. Dunkel, K. Drescher, *Nat. Phys.* **2019**, *15*, 251.
- [10] J. Huang, S. Liu, C. Zhang, X. Wang, J. Pu, F. Ba, S. Xue, H. Ye, T. Zhao, K. Li, *Nat. Chem. Biol.* **2019**, *15*, 34.
- [11] Y. Wang, B. An, B. Xue, J. Pu, X. Zhang, Y. Huang, Y. Yu, Y. Cao, C. Zhong, *Nat. Chem. Biol.* **2021**, *17*, 351.
- [12] J. K. Teschler, D. Zamorano-Sánchez, A. S. Utada, C. J. A. Warner, G. C. L. Wong, R. G. Linington, F. H. Yildiz, *Nat. Rev. Microbiol.* **2015**, *13*, 255.
- [13] O. Lieleg, M. Caldara, R. Baumgärtel, K. Ribbeck, *Soft Matter* **2011**, *7*, 3307.
- [14] K. Kovach, M. Davis-Fields, Y. Irie, K. Jain, S. Doorwar, K. Vuong, N. Dhamani, K. Mohanty, A. Touhami, V. D. Gordon, *NPJ Biofilms Microbiomes* **2017**, *3*, 1.
- [15] E. S. Gloag, G. K. German, P. Stoodley, D. J. Wozniak, *Sci. Rep.* **2018**, *8*, 9691.
- [16] J. Yan, A. Moreau, S. Khodaparast, A. Perazzo, J. Feng, C. Fei, S. Mao, S. Mukherjee, A. Košmrlj, N. S. Wingreen, B. L. Bassler, H. A. Stone, *Adv. Mater.* **2018**, *30*, 1804153.
- [17] S. G. V. Charlton, M. A. White, S. Jana, L. E. Eland, P. G. Jayatilake, J. G. Burgess, J. Chen, A. Wipat, T. P. Curtis, *J. Bacteriol.* **2019**, *201*, e00101.
- [18] A. Welker, T. Cronenberg, R. Zöllner, C. Meel, K. Siewering, N. Bender, M. Hennes, E. R. Oldewurtel, B. Maier, *Phys. Rev. Lett.* **2018**, *121*, 118102.
- [19] B. Maier, *Annu. Rev. Biophys.* **2021**, *50*, 401.
- [20] H. Cao, O. Habimana, A. Safari, R. Heffernan, Y. Dai, E. Casey, *NPJ Biofilms Microbiomes* **2016**, *2*, 5.
- [21] E. J. Nelson, J. B. Harris, J. G. Morris, S. B. Calderwood, A. Camilli, *Nat. Rev. Microbiol.* **2009**, *7*, 693.
- [22] J. C. N. Fong, K. A. Syed, K. E. Klose, F. H. Yildiz, *Microbiology* **2010**, *156*, 2757.
- [23] F. H. Yildiz, G. K. Schoolnik, *Proc. Natl. Acad. Sci. USA* **1999**, *96*, 4028.

- [24] J. C. N. Fong, K. Karplus, G. K. Schoolnik, F. H. Yildiz, *J. Bacteriol.* **2006**, *188*, 1049.
- [25] K. M. Giglio, J. C. Fong, F. H. Yildiz, H. Sondermann, *J. Bacteriol.* **2013**, *195*, 3277.
- [26] J. C. Fong, A. Rogers, A. K. Michael, N. C. Parsley, W.-C. Cornell, Y.-C. Lin, P. K. Singh, R. Hartmann, K. Drescher, E. Vinogradov, L. E. Dietrich, C. L. Partch, F. H. Yildiz, *eLife* **2017**, *6*, e1002210.
- [27] V. Berk, J. C. Fong, G. T. Dempsey, O. N. Develioglou, X. Zhuang, J. Liphardt, F. H. Yildiz, S. Chu, *Science* **2012**, *337*, 236.
- [28] J. C. N. Fong, F. H. Yildiz, *J. Bacteriol.* **2007**, *189*, 2319.
- [29] C. Absalon, K. Van Dellen, P. I. Watnick, *PLoS Pathog.* **2011**, *7*, e1002210.
- [30] S. Beyhan, F. H. Yildiz, *Mol. Microbiol.* **2007**, *63*, 995.
- [31] J. Yan, C. Fei, S. Mao, A. Moreau, N. S. Wingreen, A. Košmrlj, H. A. Stone, B. L. Bassler, *Elife* **2019**, *8*, e43920.
- [32] Z. Jiang, T. Nero, S. Mukherjee, R. Olson, J. Yan, *Front. Microbiol.* **2021**, *12*, 686793.
- [33] L. Pavlovsky, J. G. Younger, M. J. Solomon, *Soft Matter* **2013**, *9*, 122.
- [34] S. Pandit, M. Fazilati, K. Gaska, A. Derouiche, T. Nypelö, I. Mijakovic, R. Kádár, *Int. J. Mol. Sci.* **2020**, *21*, 6755.
- [35] T. Shaw, M. Winston, C. J. Rupp, I. Klapper, P. Stoodley, *Phys. Rev. Lett.* **2004**, *93*, 098102.
- [36] S. Jana, S. G. V. Charlton, L. E. Eland, J. G. Burgess, A. Wipat, T. P. Curtis, J. Chen, *NPJ Biofilms Microbiomes* **2020**, *6*, 19.
- [37] N. Billings, A. Birjiniuk, T. S. Samad, P. S. Doyle, K. Ribbeck, *Rep. Prog. Phys.* **2015**, *78*, 036601.
- [38] L. Qi, G. F. Christopher, *Rheol. Acta* **2021**, *60*, 219.
- [39] P. Shivapooja, Q. Wang, B. Orihuela, D. Rittschof, G. P. López, X. Zhao, *Adv. Mater.* **2013**, *25*, 1430.
- [40] R. H. Ewoldt, A. Hosoi, G. H. McKinley, *J. Rheol.* **2008**, *52*, 1427.
- [41] R. H. Ewoldt, P. Winter, J. Maxey, G. H. McKinley, *Rheol. Acta* **2010**, *49*, 191.
- [42] K. Hyun, M. Wilhelm, C. O. Klein, K. S. Cho, J. G. Nam, K. H. Ahn, S. J. Lee, R. H. Ewoldt, G. H. McKinley, *Prog. Polym. Sci.* **2011**, *36*, 1697.
- [43] A. C. Pipkin, *Lectures on Viscoelasticity Theory*, Springer-Verlag, New York **1972**.
- [44] K. S. Cho, K. Hyun, K. H. Ahn, S. J. Lee, *J. Rheol.* **2005**, *49*, 747.
- [45] M. Maestre-Reyna, W.-J. Wu, A. H. J. Wang, *PLoS One* **2013**, *8*, e82458.
- [46] J. Yan, C. D. Nadell, H. A. Stone, N. S. Wingreen, B. L. Bassler, *Nat. Commun.* **2017**, *8*, 327.
- [47] H. Ye, Z. Shen, Y. Li, *Comput. Mech.* **2018**, *62*, 457.
- [48] H. Ye, Z. Shen, Y. Li, *J. Fluid Mech.* **2019**, *861*, 55.
- [49] J. Jara, F. Alarcón, A. K. Monnappa, J. I. Santos, V. Bianco, P. Nie, M. P. Ciamarra, Á. Canales, L. Dinis, I. López-Montero, *Front. Microbiol.* **2021**, *11*, 3460.
- [50] E. Y. Ong, M. Ramaswamy, R. Niu, N. Y. Lin, A. Shetty, R. N. Zia, G. H. McKinley, I. Cohen, *J. Rheol.* **2020**, *64*, 343.
- [51] M. Rubinstein, R. H. Colby, *Polymer Physics*, Oxford University Press, New York **2003**.
- [52] D. Andrienko, *J. Mol. Liq.* **2018**, *267*, 520.
- [53] G. B. Jeffery, *Proc. R. Soc. London, Ser. A* **1922**, *102*, 161.
- [54] P. G. Jayathilake, B. Li, P. Zuliani, T. Curtis, J. Chen, *Sci. Rep.* **2019**, *9*, 14540.
- [55] J. Mewis, N. J. Wagner, *Adv. Colloid Interface Sci.* **2009**, *147*, 214.
- [56] M. Ganesan, S. Knier, J. G. Younger, M. J. Solomon, *Macromolecules* **2016**, *49*, 8313.
- [57] J. Yan, A. G. Sharo, H. A. Stone, N. S. Wingreen, B. L. Bassler, *Proc. Natl. Acad. Sci. USA* **2016**, *113*, E5337.
- [58] Y. Deng, M. Sun, J. W. Shaevitz, *Phys. Rev. Lett.* **2011**, *107*, 158101.
- [59] L. Hobley, C. Harkins, C. E. Macphee, N. R. Stanley-Wall, *FEMS Microbiol. Rev.* **2015**, *39*, 649.
- [60] J. Huang, S. Liu, C. Zhang, X. Wang, J. Pu, F. Ba, S. Xue, H. Ye, T. Zhao, K. Li, Y. Wang, J. Zhang, L. Wang, C. Fan, T. K. Lu, C. Zhong, *Nat. Chem. Biol.* **2019**, *15*, 34.
- [61] J. B. Hooper, K. S. Schweizer, *Macromolecules* **2005**, *38*, 8858.
- [62] S. K. Kumar, R. Krishnamoorti, *Annu. Rev. Chem. Biomol.* **2010**, *1*, 37.
- [63] S. K. Kumar, V. Ganesan, R. A. Riggleman, *J. Chem. Phys.* **2017**, *147*, 020901.
- [64] P. G. Jayathilake, P. Gupta, B. Li, C. Madsen, O. Oyebamiji, R. González-Cabaleiro, S. Rushton, B. Bridgens, D. Swailes, B. Allen, *PLoS One* **2017**, *12*, e0181965.
- [65] B. Li, D. Taniguchi, J. P. Gedara, V. Gogulancea, R. Gonzalez-Cabaleiro, J. Chen, A. S. McGough, I. D. Ofiteru, T. P. Curtis, P. Zuliani, *PLoS Comput. Biol.* **2019**, *15*, e1007125.
- [66] B. Qin, C. Fei, A. A. Bridges, A. A. Mashruwala, H. A. Stone, N. S. Wingreen, B. L. Bassler, *Science* **2020**, *369*, 71.
- [67] Q. Zhang, J. Li, J. Nijjer, H. Lu, M. Kothari, R. Alert, T. Cohen, J. Yan, *Proc. Natl. Acad. Sci. USA* **2021**, *118*, e2107107118.
- [68] J. Nijjer, C. Li, Q. Zhang, H. Lu, S. Zhang, J. Yan, *Nat. Commun.* **2021**, *12*, 6632.
- [69] K. Skorupski, R. K. Taylor, *Gene* **1996**, *169*, 47.
- [70] H. Ye, Z. Shen, W. Xian, T. Zhang, S. Tang, Y. Li, *Comput. Phys. Commun.* **2020**, *256*, 107463.
- [71] S. Plimpton, *J. Comput. Phys.* **1995**, *117*, 1.
- [72] H. Ye, Z. Shen, M. Wei, Y. Li, *Soft Matter* **2021**, *17*, 40.
- [73] W. Humphrey, A. Dalke, K. Schulten, *J. Mol. Graph.* **1996**, *14*, 33.